Lawrence Berkeley National Laboratory

Title

Pore-scale CFD simulations of clay mobilization in natural porous media due to fresh water injection

Permalink

https://escholarship.org/uc/item/46c8h4bd

Authors

Bhuvankar, Pramod
Cihan, Abdullah
Birkholzer, Jens

Publication Date

DOI

Copyright Information

Peer reviewed

Pore-scale CFD simulations of clay mobilization in natural porous media due to fresh water injection

Pramod Bhuvankar[1]†, Abdullah Cihan[1] and Jens Birkholzer[1]

[1]Energy Geosciences Division, Lawrence Berkeley Laboratory, Berkeley, CA 94720, USA

Abstract

The present work investigates mechanisms of permeability impairment as a result of low-salinity fluid injection into brine-saturated porous media containing dispersible clays. We present a computational fluid dynamics model at the pore-scale to simulate detachment, migration and straining of fine particles in porous media. The model uses an immersed boundary method to simulate the motion of clay fines in a fluid. In addition to the hydrodynamic forces, we model the Derjaguin-Landau-Verwey-Overbeek forces (DLVO) between clay fines and grains. Our simulations show the impact of the injected fluid's salinity and velocity on the concentration of clay fines retained on the grain surface. We see clay particles dislodging from the grain surface in clusters of up to 12 particles. Our simulation results also demonstrate clogging of narrow pore spaces by the detached particles from the grain surfaces.

1. Introduction

Migration of fine particles in porous media is of interest to many subsurface engineering applications such as water disposal, water treatment, well drilling, oil recovery, geothermal energy, and geological CO_2 storage (Corapcioglu *et al.* 1987; Xie *et al.* 1987; Khilar & Fogler 1998). Such applications often involve injection of lower-salinity fluids in relatively high-salinity native brine. Consequently, clay fines detach due to sharply decreasing salt concentrations near the low-salinity fluid injection wells, migrate, and finally clog the pores, which can lead to an increase in hydraulic resistance in porous media (Chequer & Bedrikovetsky 2019). This phenomenon of permeability decline is known to reduce the well injectivity (Chequer *et al.* 2018). Efforts to mitigate this problem will require an understanding of the behavior of fines in porous media. The present study focuses on permeability impairment as a result of low-salinity fluid injection into brine-saturated porous media containing dispersible non-swelling clay.

In the presence of high-salinity brine, the fine particles, ranging from $0.1\mu m$ to $10\mu m$ in size (Khilar & Fogler 1998), are bound to the pore surfaces by the influence of the Derjaguin-Landau-Verwey-Overbeek forces (DLVO) comprising of the Van der Waals, electric double layer, and Born-repulsion forces (Chequer & Bedrikovetsky 2019). These DLVO forces are also active between any two clay particles in contact. The injection of fresh water causes an expansion of the electric double layer at the grain and clay surfaces, leading to a reduction in the net force binding the fines to the grain. The injected fresh water exerts hydrodynamic drag and lift forces on the fine particles that further aid in the removal of the fine particles. When the hydrodynamic forces acting on the clay fines overcome the DLVO forces, the particles detach from the grain surface, migrate down-gradient and eventually settle. Song & Kovscek (2016) show a visualization of mobile

clay fines clogging pore spaces under low salinity conditions. It is widely noted that in porous media, the gravitational and lift forces are orders of magnitude smaller than the electrostatic and drag forces (Chequer & Bedrikovetsky 2019; Brady *et al.* 2015; Elimelech *et al.* 1995). Khilar & Fogler (1998) discuss in detail the analytical expressions for the various components of the DLVO forces for simple geometries, like spheres and plates. For more complex geometries, researchers have used the surface element integration method (SEI) proposed by Bhattacharjee & Elimelech (1997); Bhattacharjee *et al.* (1998). Chequer & Bedrikovetsky (2019) and Russell *et al.* (2019) have used the expression for Stokes drag on a sphere to approximate the drag force on clay particles.

Existing studies point to the detachment of the fine particles when the torque on the fines due to the hydrodynamic and double-layer forces exceeds that due to the Van der Waals force (Russell *et al.* 2019; Zeinijahromi *et al.* 2012). Zeinijahromi *et al.* (2012) used this approach to define a parameter called the erosion number ϵ as the ratio of the hydrodynamic to DLVO torques. They present the permeability decline as function of the said parameter ϵ. More recently, Chequer & Bedrikovetsky (2019) performed experiments to show that clay fines detach in clusters of 2 to 12 particles, and that a torque-based estimation under-predicts the detachment velocity. Existing models for representing fine migration and permeability decline rely on kinetic expressions with empirical coefficients derived from core-scale laboratory experiments (You *et al.* 2016; Chequer *et al.* 2018; Zeinijahromi *et al.* 2012).

The recent years have seen a growing interest in pore-scale computational fluid dynamics for insights into particulate flow in porous media. Developments in numerical techniques such as the immersed boundary method (Mittal & Iaccarino 2005) and tensorial penalty method (Vincent *et al.* 2014) have enabled simulations of multiple immersed particles in porous media. Su *et al.* (2019) performed 2D immersed boundary method based simulations of particulate flows in porous media reconstructed from micro-CT scans. They show that the inlet pressure increases when mobile particles clog pore spaces. They consider particles of size 150μm to 190μm, and their analysis does not included DLVO interactions between the particles and grains. Sefrioui *et al.* (2013) use the tensorial penalty method (Vincent *et al.* 2014) to simulate the motion of a spherical clay particle of radius $400n$m over a wedge. Their simulations include DLVO interactions between the clay particle and the wedge derived using the surface element integration method (Bhattacharjee & Elimelech 1997).

In summary, most existing studies on clay mobilization in porous media rely on empirical correlations constructed using lab data. The pore-scale simulation studies have either dealt with a single particle or have not taken DLVO effects into account. In the present work, we extend an immersed boundary method discussed in Bigot *et al.* (2014) to include clay-grain and clay-clay DLVO interactions. We perform 2D pore-scale computational fluid dynamics simulations to determine the detachment characteristics of the clay in response to varying the injected fluid salinity and velocity. Additionally, we conduct simulations to show the clogging mechanism by which mobile clay particles cause the permeability to decline.

2. Numerical method

2.1. *Governing equations*

In the present work we use the immersed boundary method to model the flow around the clay fines and grains. While the clay fines exist in the form of platelets, needles or flakes (Khilar & Fogler 1998), in our current work we represent them as circular (2D)
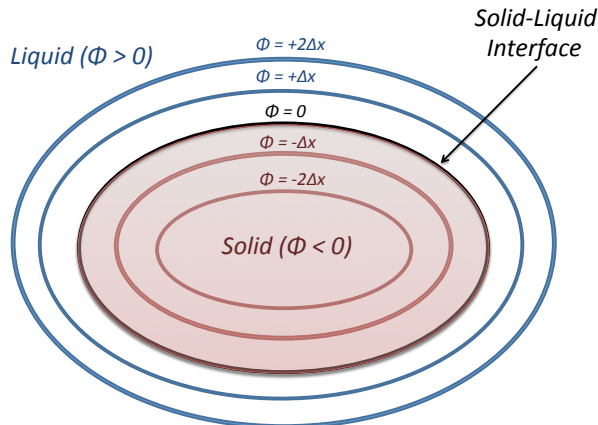
FIGURE 1. Showing the different contours of ϕ around the solid-liquid interface.

or spherical objects, as doing so will significantly simplify the numerical analysis. This representation has been used in several existing analyses of colloids in porous media (Chequer & Bedrikovetsky 2019; Bedrikovetsky *et al.* 2011; Russell *et al.* 2019; Sefrioui *et al.* 2013). Likewise, the grains are assumed to be circular (2D) in our present work.

We use a finite volume method framework to solve the incompressible Navier-Stokes equations and the continuity equation. The fractional-step method(Kim & Moin 1985) is employed to solve the said equations. Listed below are the continuity and momentum equations, respectively, in the index notation:

$$\nabla \cdot \mathbf{u} = 0, \tag{2.1}$$

$$\rho \left(\partial_t \mathbf{u} + \nabla \cdot (\mathbf{uu}) \right) = -\nabla p + \nabla \cdot \left\{ \mu \left(\nabla \mathbf{u} + (\nabla \mathbf{u})^T \right) \right\} + \rho \mathbf{g} + \rho \mathbf{F}. \tag{2.2}$$

Here, ρ is the liquid density, p is the pressure, μ is the liquid viscosity, and $\mathbf{u}$ is the velocity vector field. The computational domain has 'solid' and 'liquid' zones. The distance function ϕ is used to represent the solid-liquid interface. $\phi(\mathbf{x})$ is the shortest distance of point $\mathbf{x}$ from a solid surface. ϕ is positive outside the solid zone and negative inside. Shown in figure 1 is a schematic of solid and liquid zones separated by the zero-level set of the distance function. The $\rho \mathbf{F}$ term in the end of equation 2.2 is the immersed body force. There is a transition zone spanning 3 cells between the liquid and solid zones. We define a color function $c(\mathbf{x})$ which has a value 0 in the solid, 1 in the liquid and an intermediate value $0 < c(\mathbf{x}) < 1$ in the transition zone. The color function is defined using the distance function as:

$$c(\mathbf{x}) = \frac{1}{2} \left[1 + \tanh \left(\frac{2\phi(\mathbf{x})}{\Delta x} \right) \right]. \tag{2.3}$$

The color function is equal to 0.5 at the interface. Figure 2 shows the different zones with their color function values. The term $\rho \mathbf{F}$ in equation 2.2 is added to enforce rigid body behavior with a prescribed velocity and angular velocity in the solid section of the computational domain. Equations 2.1 and 2.2 are solved everywhere in the computational domain. The force $\mathbf{F}$ is non-zero only if $c(\mathbf{x}) < 1$, and is equal to zero everywhere else in
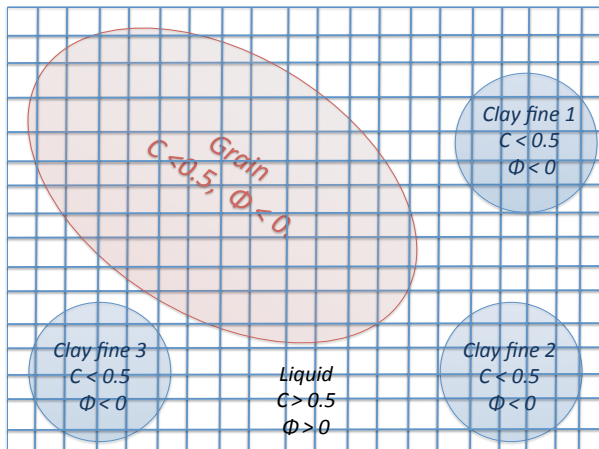
FIGURE 2. Showing the computational domain with different zones.

the liquid. The forcing function $\mathbf{F}$ is modeled as

$$\mathbf{F}(\mathbf{x}) = (1 - c(\mathbf{x})) \left[\frac{\mathbf{U}(\mathbf{x}) - \mathbf{U}^*(\mathbf{x})}{\Delta t} \right]. \tag{2.4}$$

Here, $\mathbf{U}$ is the solid velocity we wish to impose at location $\mathbf{x}$, and $\mathbf{U}^*$ is the velocity obtained in the predictor step of the fractional-step method used to solve equation 2.2. For a rigid body, we have

$$\mathbf{U} = \mathbf{u}_p + \omega_p \times (\mathbf{x} - \mathbf{x}_p). \tag{2.5}$$

$\mathbf{x}_p$ is the position of the center of mass of the solid object. If we consider a control volume around a solid zone in the domain, we have

$$\frac{d}{dt} \int_{v_p} \rho \mathbf{u} \, dv = \rho v_p \frac{d\mathbf{u}_p}{dt} = \int_{S_p} \tau . \mathbf{n} \, dS + \int_{v_p} \rho \mathbf{F} \, dv, \tag{2.6}$$

and

$$\frac{d}{dt} \int_{v_p} \rho (\mathbf{r} \times \mathbf{u}) \, dv = I \frac{d\omega_p}{dt} = \int_{S_p} (\mathbf{r} \times (\tau . \mathbf{n})) \, dS + \int_{v_p} \rho \mathbf{r} \times \mathbf{F} \, dv. \tag{2.7}$$

$\mathbf{u}$ is the velocity vector obtained from the solution of equations 2.1 and 2.2. $\mathbf{u}_p$ and ω_p are the velocity and angular velocity of the particle, respectively. v_p is the volume of the solid, ρ_p is the density of the solid, and S_p is its surface. I is the moment of inertia of the solid zone. For a solid object with the outlined interface immersed in the liquid, we have the following linear and angular momentum equations.

$$\rho_p v_p \frac{d\mathbf{u}_p}{dt} = \int_{S_p} \tau . \mathbf{n} \, dS + \rho_p v_p \mathbf{g}, \tag{2.8}$$

and

$$I_p \frac{d\omega_p}{dt} = \int_{S_p} (\mathbf{r} \times (\tau . \mathbf{n})) \, dS, \tag{2.9}$$

where I_p is the moment of inertia of the solid object. Combing equations 2.6,2.7,2.8, and 2.9 results in the following equations.

$$\frac{d\mathbf{u}_p}{dt} = \mathbf{g} - \frac{1}{(\rho_p - \rho)\,v_p} \int_{v_p} \rho \mathbf{F} dv, \tag{2.10}$$

and

$$I_p \frac{d\omega_p}{dt} = -\frac{\rho_p}{(\rho_p - \rho)} \int_{v_p} \rho(\mathbf{r} \times \mathbf{F}) dv. \tag{2.11}$$

In order to solve the discussed system of equations we first solve equations 2.10 and 2.11 to obtain the velocity and angular velocity of the solid object at the present time-step in the simulation. Then, we obtain the forcing function $\mathbf{F}$ from equations 2.5 and 2.4. We solve the Navier-Stokes equations 2.2 numerically using the fractional-step method to obtain the velocity field at the subsequent time-step. We then update the position of the solid object using $\mathbf{u}_p$ and ω_p. Using the new position of the solid, we can construct the distance function field $\phi(\mathbf{x})$, and the color function field $c(\mathbf{x})$ at all the grid points in the computational domain. Once we have this color function we can start over the process.

Two points worth mentioning are that firstly, inside the stationary grains of the porous medium, $\mathbf{u}_p$ and ω_p are equal to zero. Hence for the stationary grains we do not need to solve equations 2.10 and 2.11. However, if the solid object under consideration is a mobile clay fine, we need to solve for $\mathbf{u}_p$ and ω_p using equations 2.10 and 2.11. Secondly, if the mobile fines are circular or spherical in shape in 2D and 3D, respectively, the distance function evaluation is straightforward and given by

$$\phi^c(\mathbf{x}) = |\mathbf{x} - \mathbf{x}_c| - r_c. \tag{2.12}$$

r_c being the radius of the mobile fine. Likewise, if the grains are spherical or circular in shape with radius r_g, we have:

$$\phi^g(\mathbf{x}) = |\mathbf{x} - \mathbf{x}_g| - r_g. \tag{2.13}$$

In a system with N grains and M clay particles, we have:

$$\phi^g(\mathbf{x}) = \min\{\phi_1^g(\mathbf{x}), \phi_2^g(\mathbf{x}), .., \phi_N^g(\mathbf{x})\}, \tag{2.14}$$

and

$$\phi^c(\mathbf{x}) = \min\{\phi_1^c(\mathbf{x}), \phi_2^c(\mathbf{x}), .., \phi_M^c(\mathbf{x})\}. \tag{2.15}$$

The final distance function is given by:

$$\phi(\mathbf{x}) = \min\{\phi^c(\mathbf{x}), \phi^g(\mathbf{x})\}. \tag{2.16}$$

For a system with non-spherical grains, given the binary function $\beta(\mathbf{x})$ such that

$$\beta(\mathbf{x}) = \begin{cases} 0 & \text{if grain at } \mathbf{x}, \\ 1 & \text{otherwise,} \end{cases} \tag{2.17}$$

$\phi^g(\mathbf{x})$ is computed by following the re-initialization algorithm from the conventional level-set method for multiphase flows (Gibou *et al.* 2018; Sethian & Smereka 2003). If we define

$$\phi_0^g(\mathbf{x}) = (\beta(\mathbf{x}) - 0.5)\,\Delta x, \tag{2.18}$$

where Δx is the grid spacing for the simulation, $\phi^g(\mathbf{x})$ is the steady state solution to the PDE

$$\frac{\partial \phi^g}{\partial \tau} + \text{sgn}(\phi_0^g)(|\nabla \phi^g| - 1) = 0, \tag{2.19}$$

with the initial condition

$$\phi^g(\mathbf{x}, 0) = \phi_0^g(\mathbf{x}). \tag{2.20}$$

τ here, is the pseudo-time for the re-initialization algorithm. $\mathrm{sgn}(a)$ is $+1$ or -1 if a is positive or negative, respectively. Equation 2.19 yields a steady state solution where $|\nabla \phi^g| = 1$, which implies that it is the distance function. For a detailed account of the spatial and temporal schemes used to accurately solve equation 2.19 refer to Min (2010). Once we obtain $\phi^g(\mathbf{x})$, we can use equation 2.16 to calculate the overall distance function $\phi(\mathbf{x})$. Since the grains are stationary, ϕ^g are fixed throughout the simulation. The color function is computed using equation 2.3. In a standard level-set approach (Sethian & Smereka 2003), the distance function is advected at each time-step and reinitialized every few time-steps. There is usually some loss in volume of the solid if the level-set formulation is not conservative in nature. However, in the present approach involving spherical/circular fines we compute ϕ_i^c of the ith clay particle using $\mathbf{x}_{c,i}$ and equation 2.12 at each time-step instead of advecting it. This approach avoids any volume loss in the solid. Once we have ϕ_i^c, where $i = 1, 2, 3...M$, we compute ϕ^c and ϕ using equations 2.15 and 2.16, respectively.

2.2. *Clay-clay collision*

In the present study we assume all collisions to be perfectly inelastic in nature. Existing studies in the area of particulate flow simulations have included the lubrication force arising in the thin liquid film between colliding objects (**?**Vincent *et al.* 2014). In our work however, we do not include that force for simplicity. We use a spring-damper model to mimic collisions between any two clay particles. The said spring-damper model is activated when any two clay particles come in contact with one another. Our collision model allows any two colliding clay particles to penetrate one another by a maximum distance of one grid spacing Δx. To estimate the spring constant, we perform a scaling analysis using an idealized energy balance equation. The energy stored in the spring during compression has the same order of magnitude as the sum of the externally imposed pressure gradient's work and the kinetic energy of the clay:

$$\frac{1}{2} k_{\text{sp}} (\Delta x)^2 \sim \left| \frac{dP}{dx} \right| v_{\max} \Delta x + \frac{1}{2} \rho_p v_{\max} |u|_{\max}^2. \tag{2.21}$$

Here, $|u|_{\max}$ is the maximum magnitude of the velocity in the computational domain, and $v_{\max}$ is the volume of the largest clay particle. The second term in the equation is the work done by the characteristic force-scale in the problem. $\left| \frac{dP}{dx} \right|$ is the externally imposed pressure gradient, if any. It is to be noted that the above analysis only provides an estimate of the magnitude of k_{sp} and its exact value may have to be adjusted for stability depending on the characteristic velocity scale of the problem. To ensure that the collision is inelastic and that the clay particles do not oscillate, we define the damping coefficient to satisfy the critical damping condition as

$$c_{\text{sp}} = 2\sqrt{m_p k_{\text{sp}}} = 2\sqrt{\rho_p v_{\max} k_{\text{sp}}}. \tag{2.22}$$

We define the velocity of approach between clay particles i and j as

$$u_{ij} = (\mathbf{u}_{p,i} - \mathbf{u}_{p,j}) \cdot \mathbf{n}_{ij}, \tag{2.23}$$

where $\mathbf{n}_{ij}$ is the unit normal from particle i to j computed as

$$\mathbf{n}_{ij} = \frac{\mathbf{x}_{p,j} - \mathbf{x}_{p,i}}{|\mathbf{x}_{p,j} - \mathbf{x}_{p,i}|}. \tag{2.24}$$

Here, $\mathbf{x}_{p,i}$ and $\mathbf{x}_{p,j}$ are the positions of clay particles i and j, respectively. The spring extension is defined as

$$d = |\mathbf{x}_{p,i} - \mathbf{x}_{p,j}| - r_{p,i} - r_{p,j}, \tag{2.25}$$

$r_{p,i}$ and $r_{p,j}$ being the radii of particles i and j, respectively. The collision force $\mathbf{f}_{ij}$ on clay particle i due to a collision with clay particle j is the sum of the spring compression force and the damping force. It is activated when the distance between the two particles is less than the sum of their radii and is defined as

$$\mathbf{f}_{ij} = \begin{cases} \left(k_{\mathrm{sp}}d - c_{\mathrm{sp}}u_{ij}\right)\mathbf{n}_{ij}, & \text{if } d < 0 \\ \\ 0 & \text{otherwise.} \end{cases} \tag{2.26}$$

Consequentially, we have

$$\mathbf{f}_{ji} = -\mathbf{f}_{ij}. \tag{2.27}$$

The total collision force due to clay-clay collisions on particle i in a system with M particles is given by

$$\mathbf{F}_{\mathrm{col}} = \sum_{j=1, j\neq i}^{M} \mathbf{f}_{ij}. \tag{2.28}$$

The above term is then plugged into equation 2.45.

2.3. *Clay-grain collision*

When a moving clay particle undergoes an inelastic collision with a grain, the component of its velocity normal to the grain surface vanishes. We implement this result for clay particle i when its surface touches the grain, as defined by the criterion

$$\widehat{\phi^g}\left(\mathbf{x}_{p,i}\right) \leqslant r_{p,i}. \tag{2.29}$$

Here, $\widehat{\phi^g}\left(\mathbf{x}_{p,i}\right)$ is the value of ϕ^g interpolated at the center of particle i located at $\mathbf{x}_{p,i}$. $r_{p,i}$ is the clay particle's radius. The direction normal to the surface of the grain is given by

$$\mathbf{n}_i = \left(\frac{\nabla\phi^g}{|\nabla\phi^g|}\right)_{\mathbf{x}_{p,i}}, \tag{2.30}$$

which is evaluated at the location $\mathbf{x}_{p,i}$. When the criterion in equation 2.29 is met at time-step n, the velocity of the particle i at the subsequent time-step is given by

$$\mathbf{u}_{p,i}^{n+1} = \begin{cases} \mathbf{u}_{p,i}^n - \left(\mathbf{u}_{p,i}^n \cdot \mathbf{n}_i\right)\mathbf{n}_i, & \text{if } \left(\mathbf{u}_{p,i}^n \cdot \mathbf{n}_i\right) < 0 \\ \\ \mathbf{u}_{p,i}^n & \text{otherwise.} \end{cases} \tag{2.31}$$

2.4. *DLVO forces*

The DLVO forces in clay-clay and clay-grain interactions are significant compared to the hydrodynamic force when the clay size is in the range of 0.1-$5\mu m$. The DLVO forces are composed of the Van der Waals force, the electric double layer force, and the Born repulsion force. Since the born repulsion forces become dominant at far smaller length scales compared to the former two forces, they are neglected in the present work. Existing studies such as Russell *et al.* (2019) and Khilar & Fogler (1998) have proposed expressions for DLVO forces between clay fines and grains under the assumption that the clay particles are spherical in shape and small in size compared to the typical grain size. Since our simulations are in 2D we cannot use their proposed expressions for spherical

Property	Value
Liquid density	1000 kgm^{-3}
Clay density	2000 kgm^{-3}
Viscosity	$8.9 \times 10^{-4} \text{Pa·s}$
A	$6 \times 10^{-21} J$
e	$1.602 \times 10^{-19} C$
ϵ_0	$8.85 \times 10^{-12} \text{Fm}^{-1}$
ϵ_r	80

TABLE 1. List of material properties used in the present study

geometries.

Bhattacharjee _et al._ (1998) proposed the surface element integration (SEI) technique to evaluate the Van der Waals and electric double layer forces for arbitrary geometries. Their method involves decomposing the two surfaces into small flat plates. The interaction energy between different pairs of area elements can then be integrated to find the net interaction energy. The Van der Waals interaction energy per unit area between two flat plates is given by

$$E_V(h) = -\frac{A}{12\pi h^2}, \tag{2.32}$$

and the electric double-layer interaction energy per unit area is given by

$$E_D(h) = \frac{\epsilon_0 \epsilon_r \kappa}{2}(\zeta_1^2 + \zeta_2^2)\left(1 - \coth(\kappa h) + \frac{2\zeta_1\zeta_2}{\zeta_1^2 + \zeta_2^2}\text{csch}(\kappa h)\right). \tag{2.33}$$

Here, A is the Hamaker constant for clay-liquid-grain interactions. ϵ_0 is the permittivity of vacuum, ϵ_r is the relative permittivity of the liquid, ζ_1 and ζ_2 are the zeta potentials of the clay and grain under a given salinity. h is the distance between the two plates and the κ is the inverse Debye length. At room temperature, κ is given by (Elimelech _et al._ 1995):

$$\kappa = 0.73 \times 10^8 \sqrt{\sum C_i z_i^2}, \tag{2.34}$$

where C_i and z_i are the ionic concentration in moles/m^3 and valence, respectively, of the ith ion. The total DLVO interaction energy for the two bodies is given by

$$E_T(h) = \int\int (\mathbf{n}_1 \cdot \mathbf{k}_1)(\mathbf{n}_2 \cdot \mathbf{k}_2)(E_V(h) + E_D(h))dS, \tag{2.35}$$

where $\mathbf{n}_1$ and $\mathbf{n}_2$ are the normal to the two surfaces and $\mathbf{k}_1$ and $\mathbf{k}_2$ are the unit normal of the two plates along their respective z directions. The net DLVO force is given by

$$F_{DLVO}(h) = -\frac{\partial E_T}{\partial h}. \tag{2.36}$$

In the present work we use the zeta potential data from the work of Russell _et al._ (2019). Table 1 shows the values of e, ϵ_0, and ϵ_r used in the present study.

2.5. _Algorithm_

The algorithm we employ to solve equations 2.1, 2.2, 2.10, and 2.11, is similar to Bigot _et al._ (2014), and goes as follows:

Step 1: With the up-to-date values of $\mathbf{u}^n(\mathbf{x})$ and $\phi^n(\mathbf{x})$, compute $c^n(\mathbf{x})$.

Step 2: Compute $\mathbf{F}^n(\mathbf{x})$ by plugging $c^n(\mathbf{x})$, the individual clay particle velocities $\mathbf{u}_{p,k}^n$, and particle angular velocities $\omega_{p,k}^n$ into equations 2.4 and 2.5. Note that the grain velocity is zero.

Step 3: Use the semi-implicit fractional-step method (Kim & Moin 1985) to solve for p^{n+1} and $\mathbf{u}^{n+1}$. The x and y momentum equations are split into fractional steps as

$$\frac{u^* - u^n}{\Delta t} = \mathcal{R}_{\mathrm{diff},x}^* - \mathcal{R}_{\mathrm{con},x}^n, \tag{2.37}$$

$$\frac{u^{**} - u^*}{\Delta t} = F_x^*, \tag{2.38}$$

$$\frac{u^{n+1} - u^{**}}{\Delta t} = -\frac{1}{\rho}\left(\nabla p\right)_x^{n+1}, \tag{2.39}$$

and

$$\frac{v^* - v^n}{\Delta t} = \mathcal{R}_{\mathrm{diff},y}^* - \mathcal{R}_{\mathrm{con},y}^n, \tag{2.40}$$

$$\frac{v^{**} - v^*}{\Delta t} = F_y^*, \tag{2.41}$$

$$\frac{v^{n+1} - v^{**}}{\Delta t} = -\frac{1}{\rho}\left(\nabla p\right)_y^{n+1}, \tag{2.42}$$

respectively. The continuity equation is discretized as

$$\left(\frac{\partial u}{\partial x}\right)^{n+1} + \left(\frac{\partial v}{\partial y}\right)^{n+1} = 0. \tag{2.43}$$

Here, u and v are the x and y components of the velocity vector $\mathbf{u}$, respectively, on a staggered grid. The superscripts $n, *, **$, and $n+1$ mean that the term in question is evaluated at the current time-step, the first fractional time-step, the second fractional time-step and the subsequent time-step, respectively. $(\nabla p)_x^{n+1}$ and $(\nabla p)_y^{n+1}$ are the x and y components of the pressure gradient evaluated at the $(n+1)^{\mathrm{th}}$ time-step. $\mathcal{R}_{\mathrm{con},x}$ and $\mathcal{R}_{\mathrm{diff},x}$ are the discretizations of the convective and diffusive terms from equation 2.2, respectively, along the x direction. The same applies to $\mathcal{R}_{\mathrm{con},y}$ and $\mathcal{R}_{\mathrm{diff},y}$ along the y direction. While the temporal scheme described in equations $2.37-2.43$ is first-order in time, the same approach can be extended to higher order methods including the Runge Kutta-2 method (Butcher 2008). We use the leap-frog scheme to achieve second order accuracy.

In the current work we use a second-order central difference scheme for $\mathcal{R}_{\mathrm{diff}}$ and a second-order upwind scheme for $\mathcal{R}_{\mathrm{con}}$. Note that $\mathcal{R}_{\mathrm{diff},x}^* = \mathcal{R}_{\mathrm{diff},x}(u^*, v^n, \nu)$, and $\mathcal{R}_{\mathrm{con},x}^n = \mathcal{R}_{\mathrm{con},x}(u^n, v^n)$. Equation 2.37 is used to set up a system of equations to solve for u^*. u^* is then plugged into equation 2.38 to compute u^{**}. F_x^* is computed by using equation 2.4. u^{**} is then plugged into equation 2.39. The same process is used to set up a system of equations to solve for v^* using equation 2.40, which is subsequently used to compute v^{**} with equation 2.41. v^{**} is plugged into equation 2.42. Equations 2.39 and 2.42 are then plugged into equation 2.43 to develop a pressure poisson equation for

p^{n+1}. The solution for p^{n+1} would be stable in time if the time-step

$$\Delta t = C\frac{\Delta x}{|u|_{\max}}, \tag{2.44}$$

C being the CFL number such that $C < 1$. Since our method is semi-implicit, there is no stability criterion imposed by diffusion.

Step 3: Plug p^{n+1}, u^{**} and v^{**} into equations 2.39 and 2.42, to compute u^{n+1} and v^{n+1}, respectively.

Step 4: Update the location and velocity of the individual clay particles. The acceleration of a clay particle is given by

$$\mathbf{a}_p^n = \mathbf{g} - \frac{1}{(\rho_p - \rho)\,v_p}\int_{v_p}\rho\mathbf{F}^n dv + \frac{\mathbf{F}_{\mathrm{col}}^n + \mathbf{F}_{\mathrm{DLVO}}^n}{\rho_p v_p}. \tag{2.45}$$

$\mathbf{F}_{\mathrm{col}}$ and $\mathbf{F}_{\mathrm{DLVO}}$ are the collision force and DLVO forces, respectively, experienced from both particle-particle and particle-grain interactions. If we use a simplified first-order scheme in time, we have

$$\mathbf{u}_p^{n+1} = \mathbf{u}_p^n + \mathbf{a}_p^n \Delta t, \tag{2.46}$$

and

$$\mathbf{x}_p^{n+1} = \mathbf{x}_p^n + \mathbf{u}_p^n \Delta t + \frac{1}{2}\mathbf{a}_p^n \Delta t^2. \tag{2.47}$$

Step 5: Using the updated position of the clay particles $\mathbf{x}_p^{n+1}$, reconstruct the distance functions $\phi^c(\mathbf{x})$ and $\phi(\mathbf{x})$. Return to step 1.

We solve the resulting system of linear equations using the successive over-relaxation (SOR) method with a residue of $\epsilon = 10^{-5}$. We use a time-step of $\Delta t = 10^{-8}$ sec, which ensures stability in the solution of the pressure poisson equation and the trajectory of the clay particles.

3. Results and discussion

3.1. *Verification of the SEI method*

We consider two spheres, one made up of Kaolinite clay and the other of sandstone, both having a diameter of $800nm$, in water with an NaCl concentration of $0.024M$ at a temperature of $298K$. We compute the electric double layer and Van der Waals forces by performing surface element integration explained in subsection 2.4. We use 10000 area elements on each sphere. The analytical solution for the Van der Waals interaction energy between two spheres of the same radius r, as proposed by Elimelech *et al.* (1995) is

$$E_{VDW}^a = -\frac{Ar}{12h}. \tag{3.1}$$

The analytical electric double-layer interaction energy between two spheres of radius r with constant surface potentials as presented in Bell *et al.* (1970) is

$$E_{EDL}^a = \frac{64\pi\epsilon_0\epsilon_r r^2}{(h+2r)}\left(\frac{k_B T}{ze}\right)^2\gamma_1\gamma_2 e^{-\kappa h}, \tag{3.2}$$
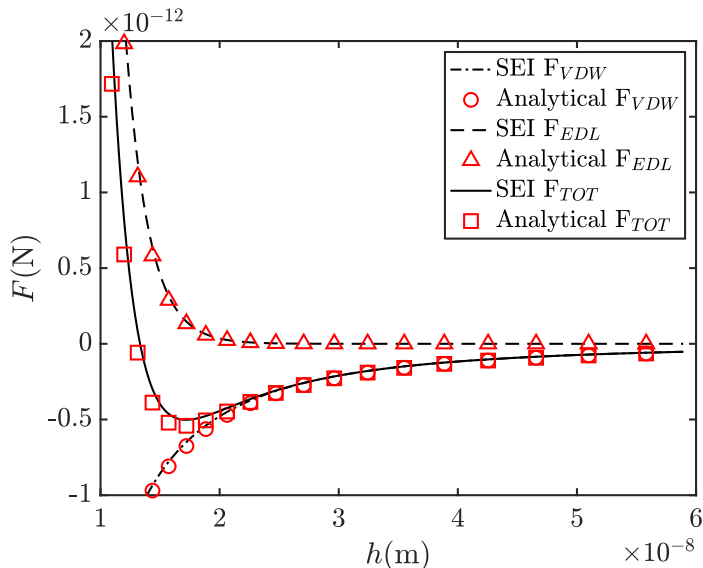
FIGURE 3. SEI based calculations and the analytical solutions of the Van der Waals, double-layer and the total DLVO forces F as a function of separation h.

where,

$$\gamma_i = \tanh\left(\frac{ze\zeta_i}{4k_BT}\right). \tag{3.3}$$

Here is the Boltzmann constant $k_B = 4.116 \times 10^{-21} J$, the electron charge is $e = 1.602 \times 10^{-19} C$, and T is the temperature in Kelvin. z is the valence of ions in the brine. ζ_1 and ζ_2 are the zeta potentials of the grain and clay, respectively. By interpolation from the data presented in the work of Russell *et al.* (2019), we have $\zeta_1 = -27.7mV$ and $\zeta_2 = -42.12mV$ as the zeta potentials. The Hamaker constant for kaolinite-water-sandstone is assumed to be $A = 6 \times 10^{-21} J$, consistent with the range of values presented in Khilar & Fogler (1998). By definition, we have the analytical forces

$$F_{EDL}^a = -\frac{\partial E_{EDL}^a}{\partial h}, \tag{3.4}$$

$$F_{VDW}^a = -\frac{\partial E_{VDW}^a}{\partial h}, \tag{3.5}$$

and

$$F_T^a = F_{EDL}^a + F_{VDW}^a. \tag{3.6}$$

Figure 3 shows the comparison between the SEI and the analytical solutions for the Van der Waals, electric double-layer, and the total DLVO forces, respectively. SEI is able to match the analytical DLVO force with 10000 elements on each sphere. Figure 3 shows that the force barrier to overcome in order to separate the two spherical particles is the absolute value of the minimum of the total force, which is $5 \times 10^{-13} N$.

3.2. *DLVO forces on circular particles*

We apply the SEI technique verified in subsection 3.1 to a 2D circular particle in an NaCl solution. We consider a circular grain of size 30μm and circular clay particles with size ranging between 0.5-3μm. The zeta potential values for kaolinite and sandstone at
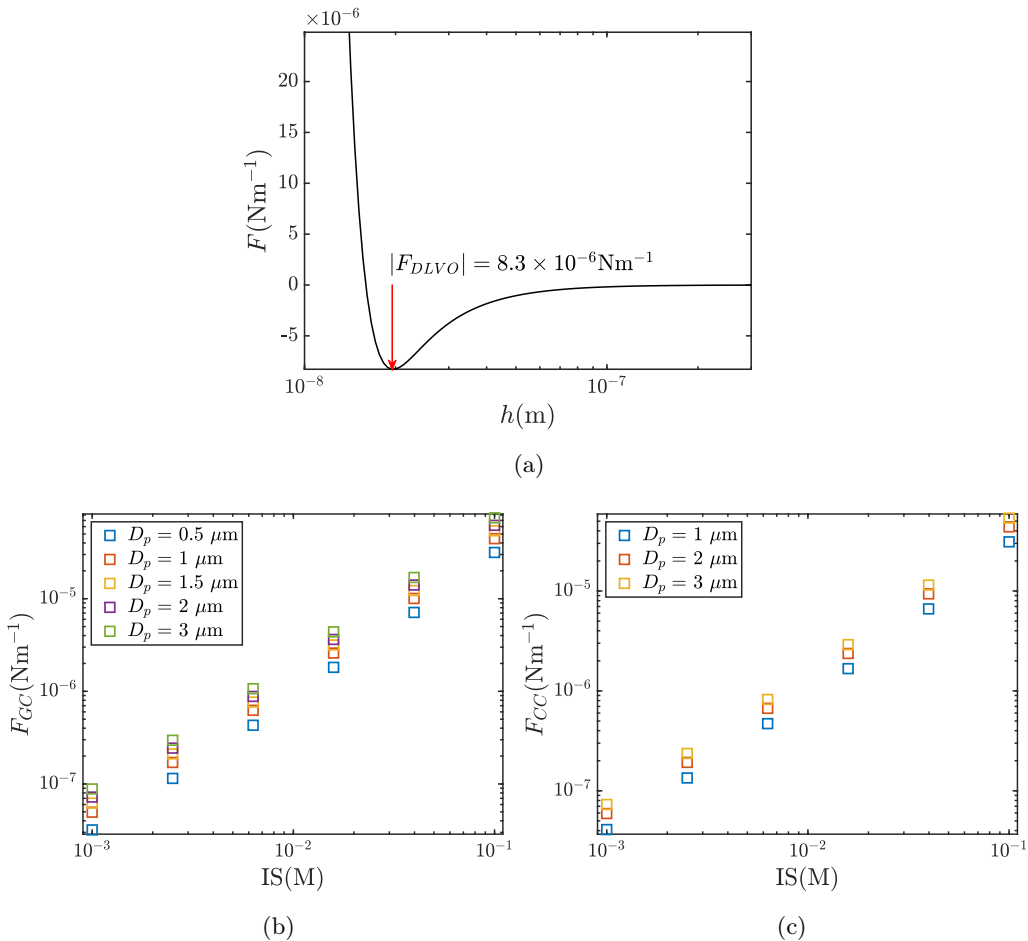
(a)

(b)

(c)

FIGURE 4. (a) DLVO force per unit length as a function of the separation between two circular surfaces. DLVO force per unit length for various ionic strengths and particle sizes for (b) grain-clay and (c) clay-clay interactions.

various ionic strengths of NaCl is interpolated from the data presented in the work of Russell *et al.* (2019). For 2D simulations on the XY plane, SEI gives us the DLVO force per unit length along the Z direction. Figure 4(a) shows the variation of the total DLVO force as a function of the distance between the two surfaces h, for an ionic strength of $0.024M$. At equilibrium, the distance between the surfaces of the two circular objects is the h where F is equal to zero. Any hydrodynamic process to separate the particle from the grain or another particle will have to overcome a force barrier of $F_{GC} = 8.3 \times 10^{-6} \mathrm{Nm}^{-1}$. We calculate the clay-clay DLVO force F_{CC} in a similar manner. Figures 4(a) and (b) show the variation of the grain-clay and clay-clay DLVO forces, respectively, with the ionic strength of the liquid $IS(M)$, for different clay particle sizes. The grain size is constant and equal to 30μm. In both the clay-clay and grain-clay cases, the force is weakened by three orders of magnitude as the brine is diluted from $0.1M$ to $0.001M$. Figure 4(a) illustrates that the grain-clay DLVO force increases in magnitude as the particle diameter increases. For a particle size of 3μm, the grain-clay force is around 1.25 times the magnitude of clay-clay forces.

The clay-clay DLVO force on particles i due to particle j is

$$\mathbf{F}_{ij}^c = \begin{cases} F_{CC}\mathbf{n}_{ij}, & \text{if } |\mathbf{x}_{p,i} - \mathbf{x}_{p,j}| \leqslant r_{p,i} + r_{p,j} + \Delta x \\ 0 & \text{otherwise}, \end{cases} \tag{3.7}$$

where, $\mathbf{n}_{ij}$ is the unit vector from particle i to j given by equation 2.24. Consequentially, we have

$$\mathbf{F}_{ji}^c = -\mathbf{F}_{ij}^c. \tag{3.8}$$

The grain-clay DLVO force on particle i is given by

$$\mathbf{F}_i^g = \begin{cases} -F_{GC}\mathbf{n}_i, & \text{if } \widehat{\phi^g}\left(\mathbf{x}_{p,i}\right) \leqslant r_{p,i} + \Delta x \\ 0 & \text{otherwise}, \end{cases} \tag{3.9}$$

where $\mathbf{n}_i$ is the unit normal to the grain surface, and $\widehat{\phi^g}\left(\mathbf{x}_{p,i}\right)$ is the grain distance function ϕ^g interpolated at the location of particle i by using bi-linear interpolation. In all our CFD simulations we assume that a force equal to F_{DLVO} acts on a clay particle whenever it is contact with another particle or a grain surface. The total force on a clay particle is thus,

$$\mathbf{F}_{\mathrm{DLVO}} = \sum_{j=1, j\neq i}^{M} \mathbf{F}_{ij}^c + \mathbf{F}_i^g. \tag{3.10}$$

This force is plugged into equation 2.45 before solving for the trajectory of the particle. For all our simulations we interpolate the different forces from the data presented in figures 4(a) and (b).

3.3. *Validation of the immersed boundary method*

We consider the benchmark problem of flow over a stationary cylinder to validate our immersed boundary method. Reynolds number Re is defined using the cylinder diameter, flow velocity, liquid viscosity and density as

$$Re = \frac{\rho U D}{\mu}. \tag{3.11}$$

Our computational domain comprises of a stationary circular obstacle of diameter D with an incoming flow of velocity U. The top and bottom edges have a free slip boundary condition while the right edge has an outflow boundary condition coupled with a fixed uniform pressure. The length and breadth of the computational domain is $10D$ and $6D$, respectively, D being the diameter of the circular object. Figure 5 shows the problem setup along with the boundary conditions imposed. We record the drag force F_{drag} on the object at steady-state and compute the drag coefficient as

$$C_D = \frac{F_{\mathrm{drag}}}{\frac{1}{2}\rho U^2 D}. \tag{3.12}$$

F_{drag} is computed by using the following equation:

$$F_{\mathrm{drag}} = -\frac{\rho_p}{(\rho_p - \rho)} \int_{v_p} \rho \mathbf{F} dv. \tag{3.13}$$

We verify our results for Reynolds numbers $Re = 10$ and 30. Existing studies on immersed boundary methods have used this problem as a benchmark to validate their techniques (**?**Bigot *et al.* 2014). Figures 6(a) and (b) show the evolution of the drag coefficient as a
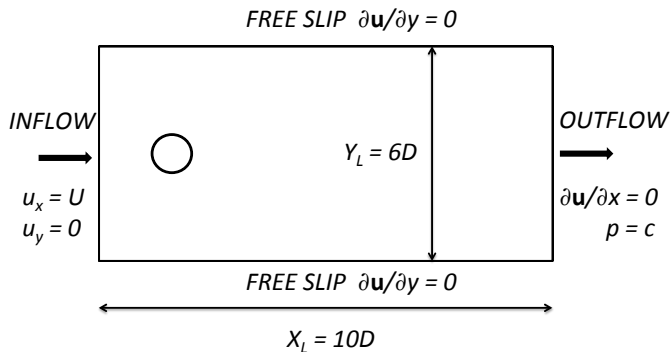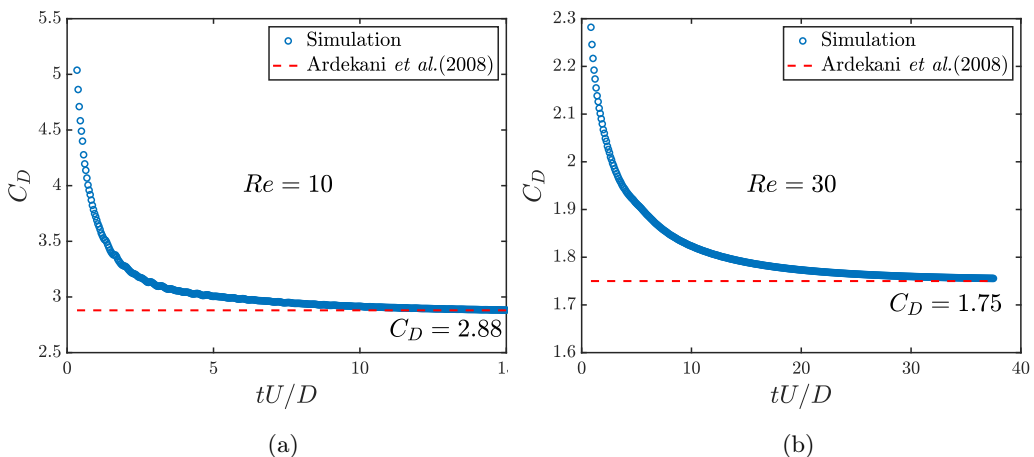
FIGURE 5. Schematic of the simulation with boundary conditions.

FIGURE 6. Drag coefficient for the cases of (a)$Re = 10$ and (b)$Re = 30$.

function of the non-dimensional time for $Re = 10$ and 30, respectively. We have a uniform grid along the X and Y directions such that there are 30 grid points across the diameter of the circular obstacle. Our results match those of **?** for both the cases. In flows through porous media, the Reynolds number is typically as low as 10^{-4} to 10^{-5}. However, the results presented above validate our numerical method and it can be used to run stokes flow simulations of conventional porous media problems.

3.4. *Grid independence*

For the sake of representation, we use green, red, and blue colors to indicate the clay, liquid, and grain phases, respectively. Note that the display color is not the same as the color function used in subsection 2.1. Since the clay particles have a size of $3\mu m$ which is an order of magnitude smaller than that of the computational domain, an important parameter to consider is the minimum number of grid points required across a particle diameter for an accurate simulation. To determine that number, we consider a test case
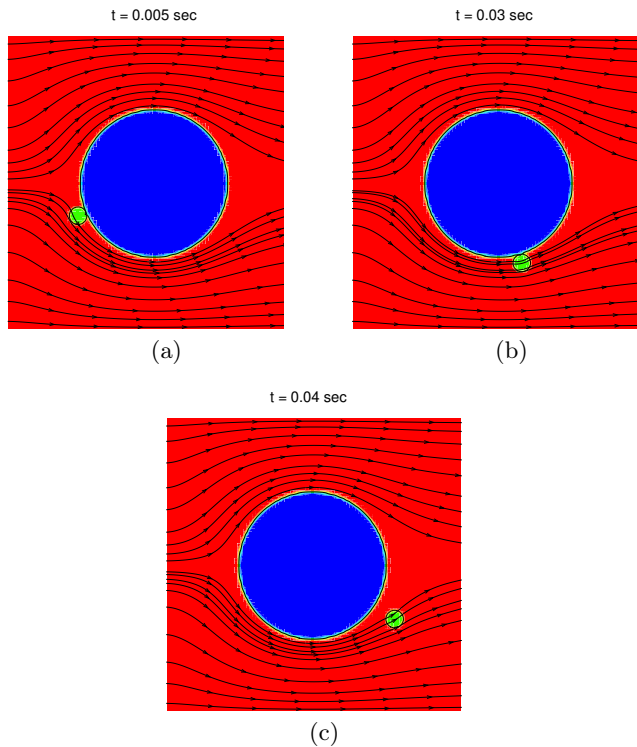
FIGURE 7. Motion of a particle initially resting on a grain for $U = 10^{-3}\text{ms}^{-1}$ at (a)$t = 5\text{ms}$, (b)30ms, and (c)40ms.

with a single grain of size $20\mu\text{m}$ and a single clay particle, as shown in figure 7(a). We have an inflow boundary condition on the left side of the domain with a velocity of $U = 10^{-3}\text{ms}^{-1}$. On the right side we have an outflow boundary condition. The top and bottom sides of the domain have free-slip boundary conditions. The dimensions of the domain are $40\mu\text{m}\times40\mu\text{m}$. There are no DLVO forces involved in this problem. As seen in figures 7(b) and (c), the particle slides on the surface of the grain and departs the grain surface. It is to be noted that the clay particle and the grain are cylindrical in shape extending into the plane of the paper. We test five different grid configurations ranging from 50×50 to 200×200. Figures 8(a),(b), and (c) show the x vs t, y vs t, and the trajectory plots of the clay particle, respectively. Overall we observe less than a 5% difference between the coarsest and the finest grid cases barring the 50×50 case for all the plots. Figure 8(a) and (b) show that beside the 50×50 case, all other cases match 200×200 case. We conclude that a grid configuration of 80×80 is fine enough to guarantee an accurate simulation of the particle motion. This grid configuration ensures 7 grid points across the clay-particle diameter. Hence, in all subsequent simulations we use 7 grid points across the clay-particle diameter.

3.5. *Clay retention*

Consider a porous medium composed of sandstone with kaolinite clay particles. We define C_p to be the initial clay content in terms of clay volume per unit volume of solids. σ is the attached clay concentration defined as the ratio of the attached clay volume to the total volume of the domain. σ_i is the initial attached clay concentration.
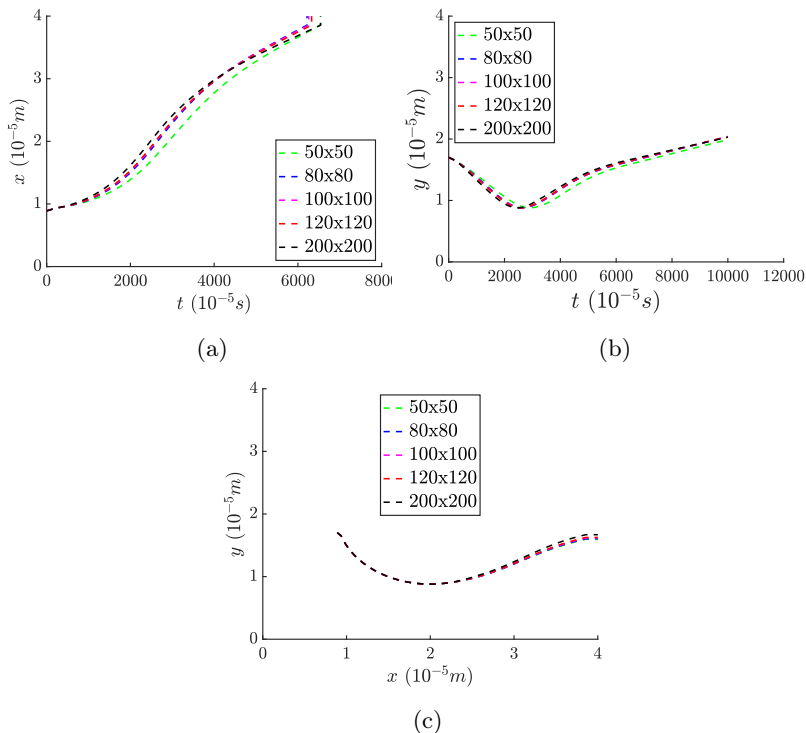
FIGURE 8. Grid independence analysis of the clay particle trajectory showing (a) x vs time, (b) y vs time, and (c) x vs y for five different grid configurations.
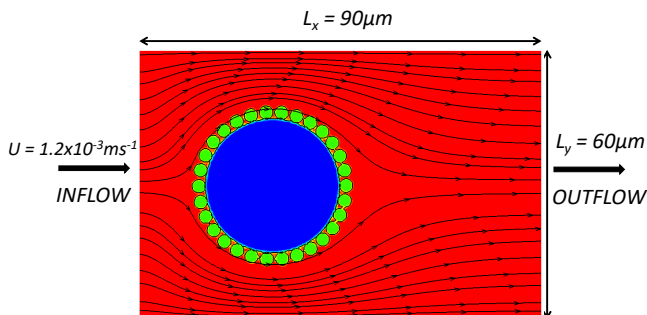

FIGURE 9. A schematic of the initial and boundary conditions for the clay retention simulations.

NaCl solutions of different ionic strengths are injected into this porous medium. As the velocity of the injected fluid $U(\mathrm{ms}^{-1})$ is increased and the ionic strength IS(M) of the fluid phase is decreased, the hydrodynamic forces dislodge the clay particles from the grain. Under these conditions (σ/σ_i) is the retention ratio. As the brine is diluted and the velocity increased, we expect the retention ratio (σ/σ_i) to decrease from 1 to 0.

Consider the setup shown in figure 9. The computational domain has dimensions $90\mu\mathrm{m}\times60\mu\mathrm{m}$, with a single grain of diameter $30\mu\mathrm{m}$ and 30 clay particles of size $3\mu\mathrm{m}$. The grain is placed at $(30\mu\mathrm{m}, 30\mu\mathrm{m})$. We have inflow and outflow boundary conditions on the left and right sides of the computational domain, respectively. The top and the bottom sides have a free-slip boundary condition. The injection velocity
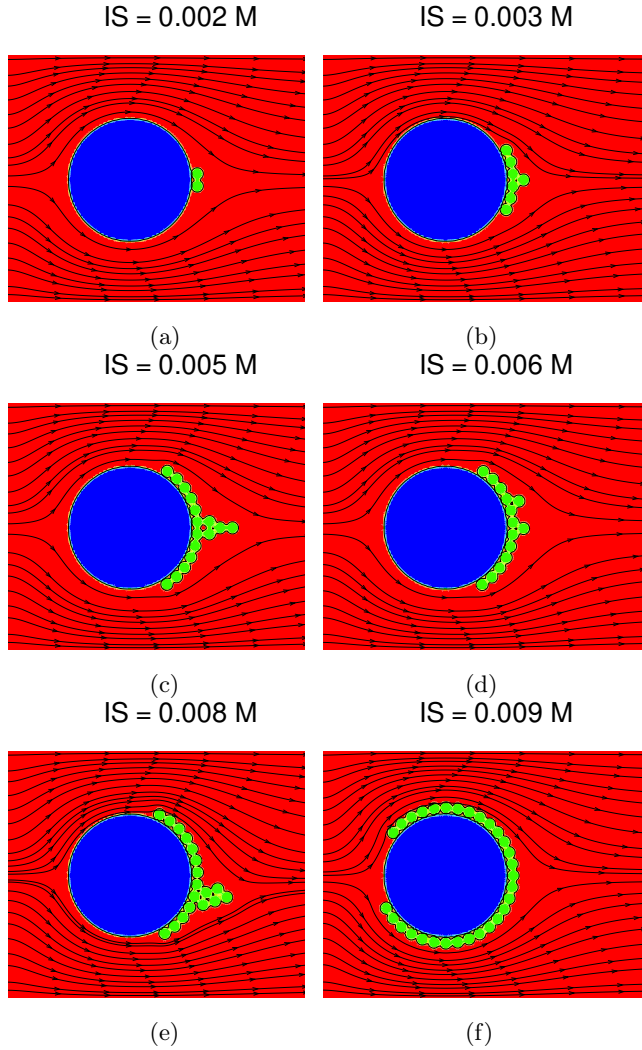
IS = 0.002 M   IS = 0.003 M

(a)   (b)

IS = 0.005 M   IS = 0.006 M

(c)   (d)

IS = 0.008 M   IS = 0.009 M

(e)   (f)

FIGURE 10. The steady-state of the simulation for ionic strength (a)$0.001M$, (b)$0.002M$, (c)$0.005M$, (d)$0.006M$, (e)$0.008M$, and (f)$0.009M$. Plots of (g)the $x-$velocity contour around the grain for $IS = 0.005M$ and (h) the color function contour as the clay particles depart at $t = 0.11$ sec.
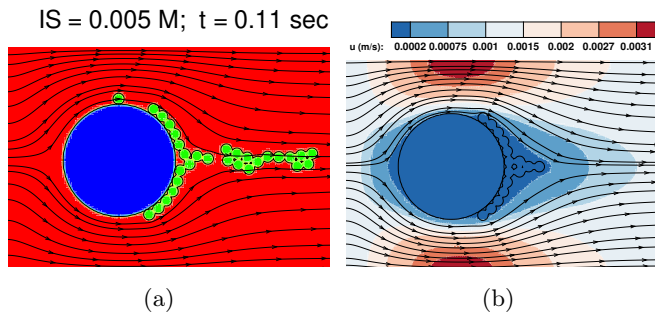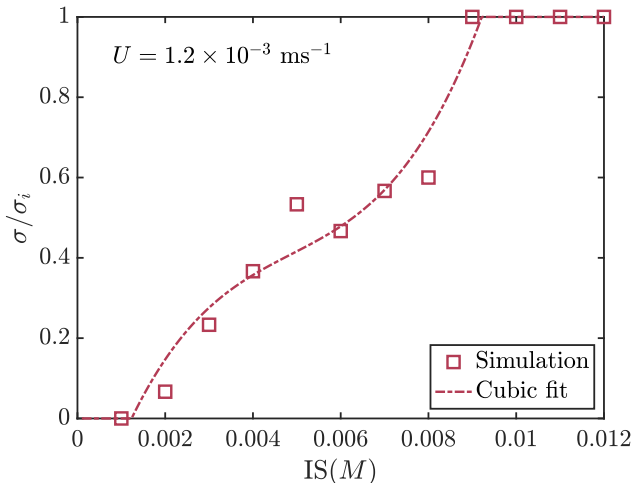
IS = 0.005 M; t = 0.11 sec

u (m/s): 0.0002 0.00075 0.001 0.0015 0.002 0.0027 0.0031

(a)   (b)

FIGURE 11. Plots of (a)the $x-$velocity contour around the grain for $IS = 0.005M$ and (b) the color function contour as the clay particles depart at $t = 0.11$ sec.

FIGURE 12. A plot of the retention ratio as a function of IS for injection velocity $U = 1.2 \times 10^{-3} \text{ms}^{-1}$.

is $U = 1.2 \times 10^{-3} \text{ms}^{-1}$. These conditions correspond to $C_p = 0.3$ and $\sigma_i = 0.04$. The properties of various materials used in our simulations are provided in table 1. All the clay particles are initially placed uniformly on the surface of the grain. For a fixed inflow velocity of $1.2 \times 10^{-3} \text{ms}^{-1}$, we simulate 12 cases of ionic strengths ranging from $0.001M$ to $0.01M$. The particle-grain DLVO force increases from $7 \times 10^{-8} \text{Nm}^{-1}$ to $5 \times 10^{-5} \text{Nm}^{-1}$ as ionic strength of NaCl is increased from $0.001M$ to $0.01M$.

Shown in figure 10(a) to (f) are the final configurations of the clay particles on the grain for cases with IS$= 0.002M$ to $0.009M$. We observe that the clay particles detach from the grain more reluctantly as the ionic strength of the solution is increased. The clay particles initially tend to roll over one another to reorient themselves downstream of the grain. Subsequently, they form triangular structures downstream which eventually break, releasing the clay particles in clusters. We see that clay particles depart in larger clusters for the higher ionic strengths. This is due to the fact that higher ionic strengths result in stronger clay-clay attractive DLVO force. An example of a departing cluster is illustrated in figure 11(a), corresponding to IS$= 0.005M$. In this example we see a cluster of 14 particles. Figure 11(b) shows the x-velocity distribution in the computational domain with low magnitudes in the vicinity of the grain.

Figure 12 is a plot of the clay retention ratio σ/σ_i from our simulations with ionic strengths ranging from $0.001M$ to $0.012M$. At ionic strengths less than $0.001M$, the retention ratio σ/σ_i is zero, meaning that all the clay particles are dislodged from the grain surface. At ionic strengths larger than $0.012M$ the retention ratio is one, meaning that all the clay particles are intact. Going from brine to fresh water we observe a transition zone between $0.09M$ and $0.001M$ where the clay retention ratio drops from 1 to 0. This means that in a porous medium with an average grain diameter 30μm, clay size 3μm, attached clay concentration $\sigma_0 = 0.04$, and an injection velocity of $U = 1.2 \times 10^{-3} \text{ms}^{-1}$, the onset of permeability decline occurs at IS$= 0.009M$. Since the initial clay content is made up of a finite number of particles, ie., 30, the transition zone is not expected to be smooth. We see from figure 12 that the variation of σ/σ_i is not entirely monotonous in the transition zone.

Figure 13 shows the variation of the retention ratio with the ionic strength for three different injection velocities. We observe that as the velocity is increased, the onset
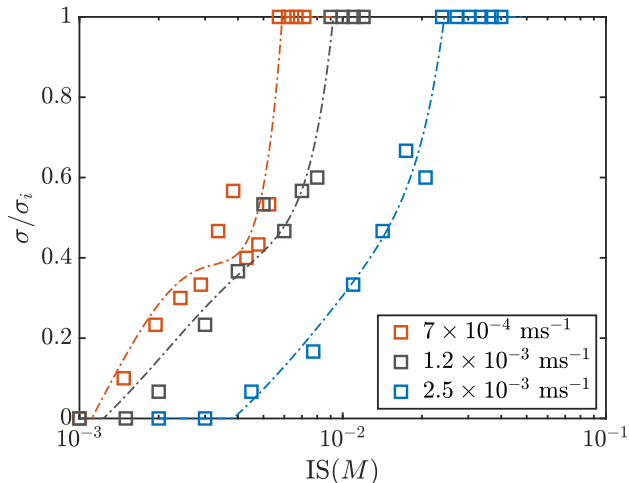
FIGURE 13. A plot of the retention ratio as a function of ionic strength for various injection velocities. The data points with black colored marker are the same as those in Figure 12
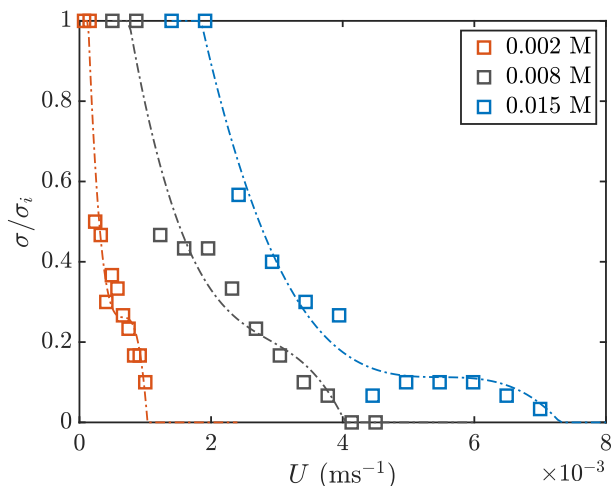

FIGURE 14. A plot of the retention ratio as a function of velocity for various ionic strengths.

of damage occurs at a higher ionic strength. It is also clear from figure 13 that the transition zone is wider for larger velocities. For a fixed ionic strength there exists a critical velocity that marks the onset clay detachment. This is evident from figure 14 which shows the retention ratio as a function of velocity at different ionic strengths. At velocities above the critical velocity value we can expect a decline in permeability. We observe that as the ionic strength is increased the critical velocity increases and the transition zone becomes wider. Russell *et al.* (2019) and Bedrikovetsky *et al.* (2011) define the critical clay concentration $\sigma_{cr}(U, \text{IS})$ to be the maximum clay concentration that can remain intact on the grain surface at a given velocity U and ionic strength IS. As per their definition, figure 14 indicates that the critical clay concentration

$$\sigma_{\text{cr}}\left(U = 1.9 \times 10^{-3}\text{ms}^{-1}, \text{IS} = 0.015M\right) = 0.04, \tag{3.14}$$

$$\sigma_{\text{cr}}\left(U = 8.6 \times 10^{-4}\text{ms}^{-1}, \text{IS} = 0.008M\right) = 0.04, \tag{3.15}$$
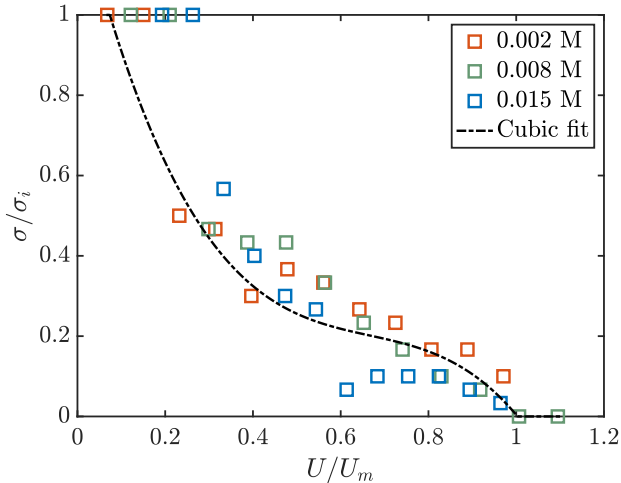
FIGURE 15. A plot of the retention ratio as a function of dimensionless velocity.

and

$$\sigma_{\text{cr}}\left(U = 1.5 \times 10^{-4}\text{ms}^{-1}, \text{IS} = 0.002M\right) = 0.04. \tag{3.16}$$

U_m is defined by Bedrikovetsky *et al.* (2011) as the minimum velocity at which no particles are attached to the grain. Figure 14 indicates that we have $U_m = 1.03 \times 10^{-3}\text{ms}^{-1}$, $4.11 \times 10^{-3}\text{ms}^{-1}$, and $7.26 \times 10^{-3}\text{ms}^{-1}$, corresponding to $IS = 0.002M$, $0.008M$, and $0.015M$, respectively. Bedrikovetsky *et al.* (2011) and Russell *et al.* (2019) proposed correlations in the form

$$\sigma \propto \left[1 - \left(\frac{U}{U_m}\right)^2\right], \tag{3.17}$$

They assumed the clay to detach as singular particles. Consistent with the observation of Chequer & Bedrikovetsky (2019) we notice that the clay departs in clusters of up to 14 particles in our simulations. Using the data from our simulations we plot (σ/σ_i) against the dimensionless velocity (U/U_m). Figure 15 shows a collapsed plot with an inflection in the transition zone. A cubic fit with the constraint $\frac{\sigma}{\sigma_i}(U_m) = 0$ results in the following correlation:

$$\frac{\sigma}{\sigma_i} = 3.16\left(1 - \frac{U}{U_m}\right)\left[\left(\frac{U}{U_m}\right)^2 - \left(\frac{U}{U_m}\right) + 0.41\right] \tag{3.18}$$

Note that equation 3.18 holds true only in the transition zone of $0.1 < \frac{U}{U_m} \leqslant 1$ and is specific to a clay size of 3μm. It is also to be noted that this result holds true for an initial clay concentration of $\sigma_i = 0.04$. In this case when $\frac{U}{U_m} < 0.1$, we have $\sigma = \sigma_i$.

It is worth mentioning that for macroscopic porous media simulations, there exist equilibrium based (Bedrikovetsky *et al.* 2011) and kinetic based techniques to model the clay fine concentration. The equilibrium model assumes a maximum clay fine retention concentration that depends on the ratio of the drag force to the normal force on the clay fine. The kinetic approach uses the capture and release rates of the clay fines. These release and capture rates are usually fine-tuned to fit experimental data. Recently, Cihan *et al.* (2021) modeled the clay fine release rate as a step function of the critical velocity and the critical salinity. The clay fine capture rate is usually modeled by using
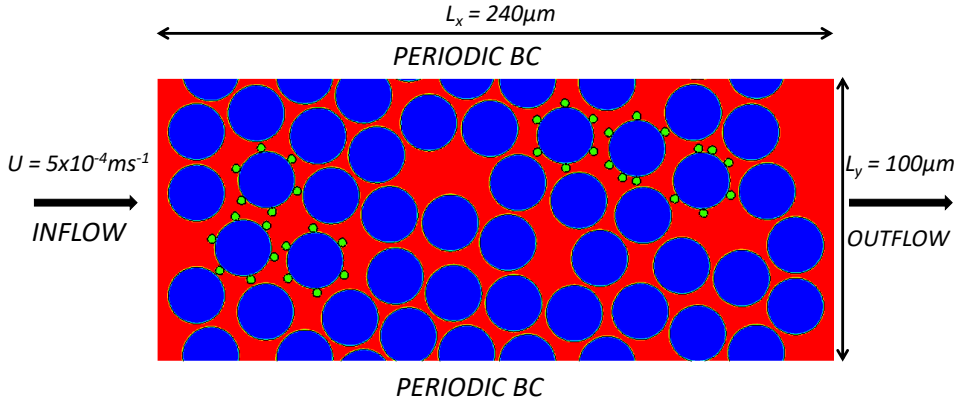
FIGURE 16. A schematic of the porous medium flow simulation showing the initial and boundary conditions.

the classical filtration theory. The CFD technique presented in our study can be used to determine the critical salinity and critical velocity values. Additionally, it can be used to determine the maximum retention concentration of the clay fines and to fine-tune the kinetic release and capture rates. It is worth noting that several additional simulations will have to be conducted using our numerical method to extensively cover the parameter space. The expansion of the parameter space to include additional variables such as porosity, fine size distribution, and the grain size distribution, is beyond the scope of the present work.

3.6. *Mechanism of permeability decline*

The permeability decline upon fresh water injection is understood to occur as a result of the filtration process of the mobile clay particles in the porous medium. This phenomenon has been investigated in detail by existing studies such as Pang & Sharma (1997), Russell *et al.* (2019), Chequer *et al.* (2018), Khilar & Fogler (1998). The colloidal filtration theory (Herzig *et al.* 2004; Tufenkji 2007) is often used to estimate the permeability decline with empirically determined capture and release coefficients. If a mobile clay particle encounters a pore-space smaller than its size, it clogs the pore-space leading to a local pressure build-up. The cumulative effect of this phenomenon results in the overall permeability decline. To illustrate this process, we setup a simulation as shown in figure 16.

The computational domain has dimensions 240μm$\times100\mu$m with inflow and outflow boundary conditions on the left and right boundaries, respectively. The injection velocity is kept constant at $U = 5 \times 10^{-4}$ms^{-1}. The top and bottom boundaries have the periodic boundary condition. The porous medium is constructed using 42 circular grains of size 20μm. The concentration of the attached clay particles is initialized as $\sigma_i = 0.01$. The diameter of the clay particles is chosen to be 3μm. All the clay particles are initially distributed uniformly on the surfaces of six grains. We use an algorithm that inputs 42 random values for locations of the grains and initializes them under the constraint that the closest distance between any two grain surfaces has to be 1μm at a minimum. Also, the closest distance between a clay carrying grain surface and a neighboring grain surface has to be 3μm at minimum. This allows the released clay particles to experience

some extent of mobilization before clogging the pores. To achieve the randomized grain configuration with the aforementioned separation constrained, we randomly initialize position $\mathbf{x}_{g,i}$, of grains $i = 1, 2, .., 42$ followed by implementing Algorithm 1.

The porosity of this system is $\psi = 0.55$. All the random numbers are generated using a

---

Algorithm 1: Randomized locations of 42 grains with the desired separation

---

Result: $\mathbf{x}_{g,i}$

$D = 20\mu m$;

$d_{\min}^i = 2.5\mu m \ \forall \ i \leqslant 6$; // Clay carrying grains

$d_{\min}^i = 0.5\mu m \ \forall \ i > 6$;

$\alpha = 0.01$;

Flag=0;

while $Flag = 0$ **do**

    counter = 0;

    $\Delta\mathbf{x}_{g,i} = 0 \ \forall \ i \leqslant 42$;

    for $i = 1$ **to** 41 **do**

        for $j = i + 1$ **to** 42 **do**

            $d_{i,j} = |\mathbf{x}_{g,i} - \mathbf{x}_{g,j}| - (D + d_{\min}^i + d_{\min}^j)$;

            if $d_{i,j} < 0$ **then**

                counter := counter+1;

                $\Delta\mathbf{x}_{g,i} := \Delta\mathbf{x}_{g,i} + \alpha(\mathbf{x}_{g,i} - \mathbf{x}_{g,j})$;

                $\Delta\mathbf{x}_{g,j} := \Delta\mathbf{x}_{g,j} - \alpha(\mathbf{x}_{g,i} - \mathbf{x}_{g,j})$;

            end

        end

    end

    for $i = 1$ **to** 42 **do**

        $\mathbf{x}_{g,i} := \mathbf{x}_{g,i} + \Delta\mathbf{x}_{g,i}$;

    end

    if $counter = 0$ **then**

        $Flag = 1$;

    end

end

---

uniform random distribution. We use a 480×200 grid configuration, which is sufficient to resolve the clay particles according to the criterion discussed in sub-section 3.4. The pressure drop across the medium is calculated by averaging the inlet pressure along the y-direction and subtracting the constant outlet pressure from it. We consider ionic strengths of the injected fluid ranging from $IS = 0.001M$ to $0.08M$.

Figure 17 shows the initial configuration on the left and the final configurations for IS $= 0.001M$ and IS $= 0.08M$ on the top-right and bottom-right, respectively. We note that in the case of IS $= 0.001M$ more clay particles detach from their original grain surface compared to the IS $= 0.08M$ case. In the latter case we see that some clay particles reorient themselves behind their original grains. We also note that in the case of IS $= 0.08M$ more clay particles are clustered together in their final state compared to the IS $= 0.001M$ case. This is due to the higher clay-clay attractive DLVO forces in the former case. Due to the lower magnitude of attractive clay-clay and clay-particle DLVO forces in the IS $= 0.001M$ case, it has a greater mobilization of the clay particles compared to IS $= 0.08M$. As a result, four pore throats are clogged in the IS$= 0.08M$ case and ten pore throats are clogged in the IS $= 0.001M$ case, as is evident from figure
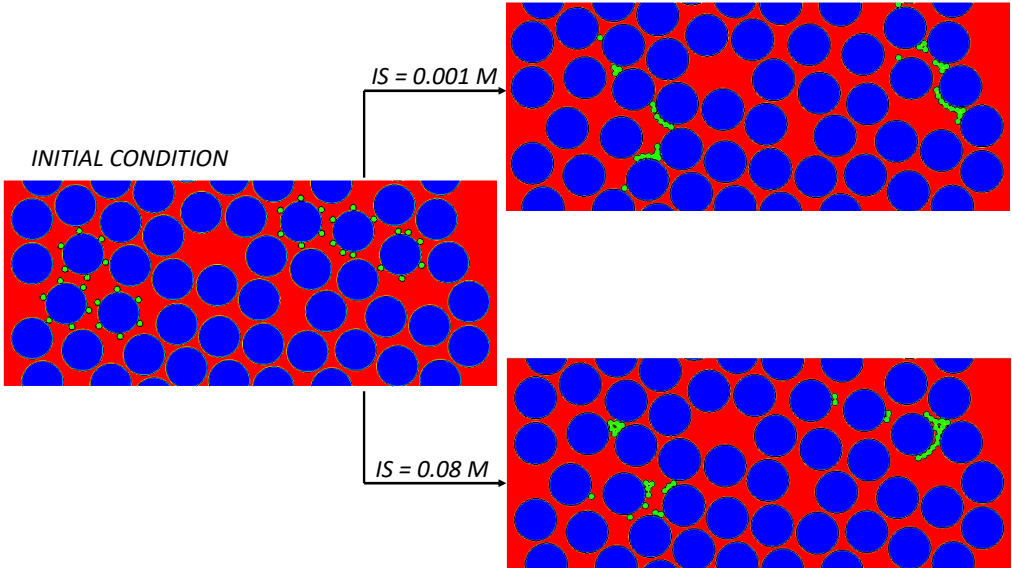
FIGURE 17. Left: The initial condition of the simulation. Right: The steady state solution for $IS = 0.001M$ on top and $IS = 0.08M$ at the bottom.
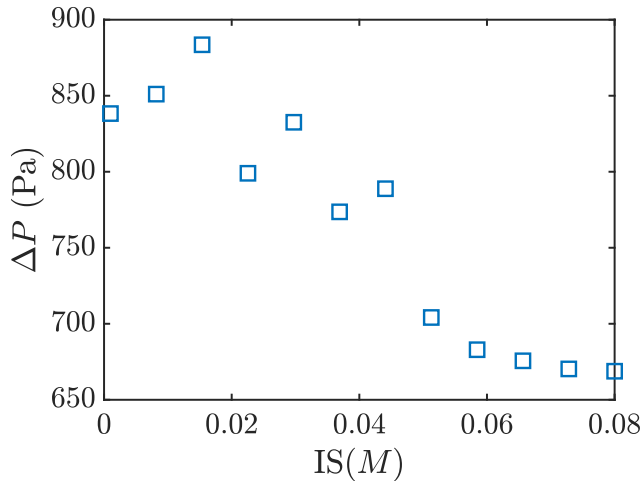

FIGURE 18. Pressure difference between the inlet and outlet for various ionic strengths.

17. This type of pore clogging can be seen in the SEM images presented in the work of Chequer & Bedrikovetsky (2019).

Figure 18 shows the pressure difference ΔP between the inlet and the outlet at the steady state for the different ionic strengths simulated. As the salinity of the fluid is decreased from IS $= 0.08M$ to $0.001M$ we observe that the pressure drop ΔP increases. We also observe that the increase in ΔP becomes more pronounced as the salinity is decreased below IS $= 0.05M$. We see a difference of up to 216 Pa in ΔP as the salinity of the fluid is decreased from IS $= 0.08M$ to IS $= 0.001M$. This increase in ΔP is caused by the clogged pore throats seen in the upper-right section compared to the lower-right section of figure 17. When clay particles clog the pore throats they increase the local tortuosity of the porous medium, thereby increasing the overall resistance to the flow. We also note
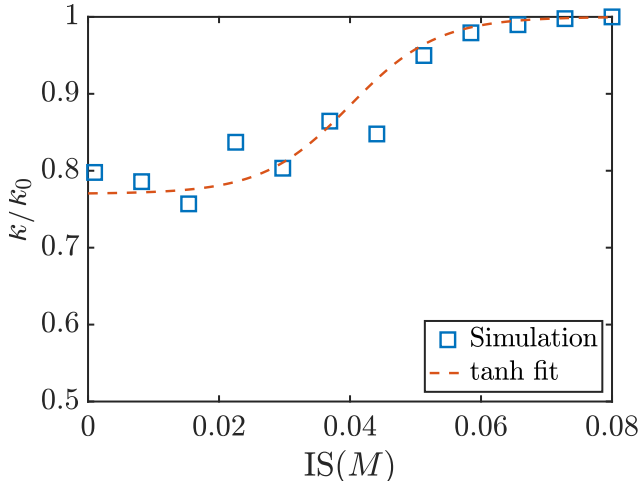
FIGURE 19. The decline in permeability k/k_0 as a function of salinity IS(M).

that for IS $\leqslant 0.04M$ the variation of ΔP is not smooth. The reason for this noise is that there is an uncertainty associated with the final positions of the clay particles as they become more mobile. The steady-state pressure drop is a function of the final positions of the various clay particles, and since figure 18 is based on a single realization of the porous medium, it is understandable that the pressure drop trend is not smooth at the lower salinity values. We can expect a smoother trend for the lower values of salinity in figure 18 if we carry out multiple simulations with different realization of the porous medium with the same values of σ_i and ψ followed by averaging the pressure drops. Since the aim of the present work is to demonstrate the physical mechanism of permeability decline, the said analysis is out of scope for our study. For a fixed injection velocity of $U = 5 \times 10^{-4}\text{ms}^{-1}$, we can express the permeability ratio $\frac{k}{k_0}$ as

$$\frac{k}{k_0} = \frac{\Delta P_0}{\Delta P}, \tag{3.19}$$

where k_0 and ΔP_0 are the permeability and pressure drop, respectively at IS $= 0.08M$. k is the permeability. Figure 19 shows the decline in permeability as the salinity is decreased from $0.08M$ to $0.001M$. We see a decline in the permeability by up to 23% in the range of salinity simulated. The red dashed line in figure 19 show a tanh fit on the simulated data points.

4. Conclusion

An immersed boundary method based numerical technique has been developed to carry out pore-scale simulations of mobile clay particles in porous media. The numerical method was validated by comparison with benchmark results from literature. The numerical method is able to incorporate the DLVO forces that act between clay particles and the grain surfaces. The surface element integration method has been verified by comparison with the analytical DLVO force between two spheres. Our simulations of flow over a clay-laden grain showed that for a given velocity there is a range of ionic strengths in which the clay retention ratio falls from 1 to 0. This range becomes narrow as the velocity is decreased. For a fixed ionic strength, our simulations showed that the clay retention ratio decreases as the velocity is increased. We also found that the retention ratio plots

for all values of ionic strengths simulated collapse into a single plot when the velocity is normalized using the cutoff velocity U_m. Contrary to the assumption made by existing models of clay detachment, we found the clay particles to depart in large clusters of up to 14 particles. This is in line with the findings of Chequer & Bedrikovetsky (2019) who observed the clay particles to depart in clusters of 2 to 12 particles. Additionally, we performed simulations of an idealized porous medium containing a clay concentration of $\sigma_i = 0.01$ for a range of ionic strength and a single injection velocity. Our simulations showed a decline in permeability of up to 23% as the salinity is reduced from IS $= 0.08M$ to $0.001M$. The onset of significant decline in permeability was found to occur at IS $= 0.05M$.

The next step in this study would be to extend the 2D numerical method to 3D in order to study 3D porous media. The correlations derived from said 3D simulations between the permeability, injection velocity, ionic strength and clay concentration can then be integrated into Darcy flow simulations carried out at much larger length scales. The future work in this study will also involve an examination of more heterogeneous porous media and the effects of clay particle size distributions on clay retention and permeability decline. It is also of interest to examine the effect of clay particle shapes on the detachment characteristics and permeability decline.

5. Acknowledgements

REFERENCES

BEDRIKOVETSKY, P., SIQUERA, F. D., FURTADO, C. A. & SOUZA, A. L. S. 2011 Modified particle detachment model for colloidal transport in porous media. *Transport in Porous Media* pp. 86:353–383.

BELL, G. M., LEVINE, S. & MCCARTNEY, L. N. 1970 Approximate methods of determining the double-layer free energy of interaction between two charged colloidal spheres. *Journal of Colloid Interface Science* **33**, 335–359.

BHATTACHARJEE, S. & ELIMELECH, M. 1997 Surface element integration: a novel technique for evaluation for evaluation of dlvo interaction between a particle and a flat plate. *Journal of Colloid Interface Science* **193** (2), 273–285.

BHATTACHARJEE, S., ELIMELECH, M. & BORKOVEC, M. 1998 Dlvo interaction between colloidal particles: Beyond derjaguin's approximation. *Croatica Chemica Acta* **71**, 12.

BIGOT, B., BONOMETTI, T., LACAZE, L. & THUAL, O. 2014 A simple immersed-boundary method for solid-fluid interaction in constant and stratified-density flows. *Computers and Fluids* **97**, 126–142.

BRADY, P. V., MORROW, N. R., FOGDEN, A., DENIZ, V. & LOAHARDJO, N. 2015 Electrostatics and the low salinity effect in sandstone reservoirs. *Energy Fuels* **29** (2), 666–677.

BUTCHER, J. C. 2008 Numerical methods for ordinary differential equations, new york. *John Wiley & Sons* .

CHEQUER, L. & BEDRIKOVETSKY, P. 2019 Suspension-colloidal flow accompanied by detachment of oversaturated and undersaturated fines in porous media. *Chemical Engineering Science* **198**, 16–32.

CHEQUER, L., VAZ, A. & BEDRIKOVETSKY, P. 2018 Injectivity decline during low-salinity waterflooding due to fines migration. *Journal of Petroleum Science and Engineering* **165**, 1054–1072.

CIHAN, A., PETRUSAK, R., BHUVANKAR, P., ALUMBAUGH, D., TRAUTZ, R. & BIRKHOLZER, J. T. 2021 Permeability decline by flay fines migration around a low-salinity fluid injection well. *Groundwater https://doi.org/10.1111/gwat.13127* .

CORAPCIOGLU, M. Y., ABBOUD, N. M. & HARIDAS, A. 1987 Governing equations for particle transport in porous media. *Advances in Transport Phenomena in Porous Media, Martinus Nijhoff Publishers, Dordrecht* .

ELIMELECH, M., GREGORY, J. & JIA, X. 1995 Particle Deposition and Aggregation: Measurement, Modelling and Simulation. Butterworth-Heinemann.

GIBOU, F., FEDKIW, R. & OSHER, S. 2018 A review of level-set methods and some recent applications. *Journal of Computational Physics* **353**, 82–109.

HERZIG, J. P., LECLERC, D. M. & GOFF, P. LE 2004 Flow of suspensions through porous media–application to deep filtration. *Journal of Industrial and Engineering Chemistry* **244**, 151–165.

KHILAR, K. C. & FOGLER, H. S. 1998 Migrations of fines in porous media. *Kluwer Academic Publishers, Dordrecht* .

KIM, J. & MOIN, P. 1985 Application of a fractional-step method to incompressible navier-stokes equations. *Journal of Computational Physics* **59** (2), 308–323.

MIN, C. 2010 On reinitializing level set functions. *Journal of Computational Physics* **229**, 2764–2772.

MITTAL, R. & IACCARINO, G. 2005 Immersed boundary methods. *Annual Review of Fluid Mechanics* pp. 37:239–61.

PANG, S. & SHARMA, M. M. 1997 A model for predicting injectivity decline in water-injection wells. *Society of Petroleum Engineers* **12** (3), 194–201.

RUSSELL, T., PHAM, D., NEISHABOOR, M. T., BADALYAN, A., BEHR, A., GENOLET, L., KOWOLLIK, P., ZEINIJAHROMI, A. & BEDRIKOVETSKY, P 2019 Suspension-colloidal flow accompanied by detachment of oversaturated and undersaturated fines in porous media. *Chemical Engineering Science* **198**, 16–32.

SEFRIOUI, N., AHMADI, A., OMARI, A. & BERTIN, H. 2013 Numerical simulation of retention and release of colloids in porous media at the pore scale. *Colloids and Surfaces A: Physicochemical and Engineering Aspects, Elsevier* pp. 33–40.

SETHIAN, J. A. & SMEREKA, P. 2003 Level set methods for fluid interfaces. *Annual Review of Fluid Mechanics* pp. 35:341–72.

SONG, W. & KOVSCEK, A. R. 2016 Direct visualization of pore-scale fines migration and formation damage during low-salinity waterflooding. *Journal of Natural Gas Science and Engineering* **34**, 1276–1283.

SU, J., CHAI, G., WANG, L., CAO, W., GU, Z., GU, Z., CHEN, C. & ZU, Z. Y. 2019 Pore-scale direct numerical simulation of particle transport in porous media. *Chemical Engineering Science* **199**, 613–627.

TUFENKJI, N. 2007 Colloid and microbe migration in granular experiments: a discussion of modelling methods. In *Colloidal Transport in Porous Media* (ed. F.H.Frimmel, F.C.Flemming & F.von der Kammer), , vol. 244, pp. 119–142. Berlin: Springer-Verlag.

VINCENT, S., DE MOTTA, J. C. B., SARTHOU, A., ESTIVALEZES, J., SIMONIN, O. & CLIMENT, E. 2014 A lagrangian vof tensorial penalty method for the dns of resolved particle-laden flows. *Journal of Computational Physics* **256**, 582–614.

XIE, Q., SAEEDI, A., PIANE, C. D., ESTEBAN, L. & BRADY, P. V. 1987 Fines migration

during CO2 injection: Experimental results interpreted using surface forces. *International Journal of Greenhouse Gas Control* **65**, 32–39.

You, Z., Yang, Y., Badalyan, A., Bedrikovetsky, P. & Hand, M. 2016 Mathematical modelling of fines migration in geothermal reservoirs. *Geothermics* **59**, 123–133.

Zeinijahromi, A., Vaz, A. & Bedrikovetsky, P. 2012 Well impairment by fines migration in gas fields. *Journal of Petroleum Science and Engineering* **88–89**, 125–135.